

JGR Solid Earth

RESEARCH ARTICLE

10.1029/2021JB021758

Special Section:

Ophiolites and Oceanic Lithosphere, with a focus on the Samail ophiolite in Oman

Key Points:

- High disequilibrium conditions induce skeletal awaruite growth during continental serpentinization
- Pentlandite dissolution creates fluid pathways and nutrients for microbial life
- Sulfur isotope compositions document ocean floor and subsequent continental serpentinization processes

Supporting Information:

Supporting Information may be found in the online version of this article.

Correspondence to:

E. M. Schwarzenbach,
esther.schwarzenbach@fu-berlin.de

Citation:




Schwarzenbach, E. M., Vrijmoed, J. C., Engelmann, J. M., Liesegang, M., Wiechert, U., Rohne, R., & Plümper, O. (2021). Sulfide dissolution and awaruite formation in continental serpentinization environments and its implications to supporting life. *Journal of Geophysical Research: Solid Earth*, 126, e2021JB021758. <https://doi.org/10.1029/2021JB021758>

Received 20 JAN 2021
Accepted 31 MAR 2021

© 2021. The Authors.

This is an open access article under the terms of the [Creative Commons Attribution](#) License, which permits use, distribution and reproduction in any medium, provided the original work is properly cited.

Sulfide Dissolution and Awaruite Formation in Continental Serpentinization Environments and Its Implications to Supporting Life

E. M. Schwarzenbach¹ , J. C. Vrijmoed¹, J. M. Engelmann¹, M. Liesegang¹ , U. Wiechert¹, R. Rohne¹, and O. Plümper² 

¹Institute of Geological Sciences, Freie Universität Berlin, Berlin, Germany, ²Department of Earth Sciences, Utrecht University, Utrecht, The Netherlands

Abstract Serpentinization environments are key locations that support microbial communities by the abiogenic formation of reduced species associated with peridotite alteration. Here we studied partially serpentinized peridotites from the Chimaera seeps (Turkey), an active continental serpentinization system that vents highly methane-rich fluids, to investigate the impact of water-rock interaction on the sulfide and metal mineralogy and its implications on supporting microbial communities. Using high-resolution scanning electron microscopy, electron microprobe analysis, and transmission electron microscopy we found diverse pentlandite decomposition features with precipitation of secondary sulfides including millerite, heazlewoodite, as well as Cu-bearing sulfides, native Cu, and awaruite (Ni₃Fe). Awaruite forms dense veinlets to single crystal platelets tens of nanometers in size, which is formed by desulphurization of pentlandite. In addition, the nanometer-sized awaruite platelets are intimately intergrown with serpentine suggesting its growth during peridotite alteration by a dissolution-precipitation process, likely associated with the interaction of methane- and H₂-rich but highly sulfur-undersaturated fluids. Based on sulfur isotope signatures we infer a mantle and mid-ocean ridge origin of the sulfide minerals associated with the first stage of partial serpentinization and awaruite formation. Subsequent and ongoing continental fluid-rock interaction causes significant sulfide decomposition resulting in the formation of porosity and the release of, amongst others, H₂S and Fe. These species may likely provide a source of nutrients for active microbial communities in these comparatively nutrient-starved, low-temperature continental serpentinization environments.

1. Introduction

Metal and sulfide minerals in ultramafic rocks are ideal tracers for fluid-rock interaction processes. During hydrothermal alteration of ultramafic rocks—the so-called serpentinization reaction where the primary mantle minerals olivine and pyroxene are converted to serpentine, magnetite, talc, and brucite—H₂ is produced due to ferrous iron oxidation (Klein et al., 2009; McCollom et al., 2016). Simultaneously, H₂ can react abiogenically with CO₂ or CO to produce CH₄ and higher hydrocarbons following Fischer-Tropsch Type and Sabatier reactions (e.g., Etiope et al., 2011). Associated with variations in water-rock ratios during ongoing serpentinization and rock fracturing, this imparts strong variations in fluid redox conditions, i.e., variations in *f*O₂, *f*H₂, and *f*S₂ conditions controlling the opaque mineralogy (Foustoukos et al., 2015; Frost, 1985; Klein & Bach, 2009). Effectively, changes in *f*O₂ and *f*S₂ cause precipitation of secondary opaque phases and/or decomposition of primary mantle sulfides (Alt & Shanks, 1998; Schwarzenbach et al., 2012). In fact, serpentinization environments are among the most reducing environments found on Earth allowing for formation and stabilization of native metals and metal alloys, for example, by desulfurization of magmatic pentlandite (e.g., Frost, 1985; Klein & Bach, 2009; Schwarzenbach, Gazel, & Caddick, 2014). Simultaneously, abiogenically produced H₂ and/or CH₄ as well as other reduced carbon species, produced as a result of the serpentinization process, together with oxidants such as sulfate or CO₂, provide an ideal energy source for chemolithoautotrophic communities living at sites of active serpentinization (e.g., Brazelton et al., 2006; Kelley et al., 2005; Lang et al., 2018; McCollom, 2007). In this regard, these systems have gained increasing interest in the study of the evolution of life on Earth and in the search for life on other planets and planetary bodies (Martin & Russell, 2007; Russell et al., 2010; Vance & Melwani Daswani, 2020). The detection of

H₂ and CH₄ in the atmosphere of Saturn's icy moon Enceladus offers further evidence for serpentinization providing energy for extraterrestrial microbial life (Taubner et al., 2018).

Active sites of serpentinization have been found in oceanic settings where mantle rock is exposed to seawater near ultra-slow to slow spreading mid-ocean ridges (e.g., Kelley et al., 2001) and in continental sites where meteoric water circulates through ultramafic rocks that have been emplaced on the continent (e.g., Morrill et al., 2013; Sanchez-Murillo et al., 2014; Schrenk et al., 2013). At these sites, ongoing, low-temperature serpentinization is documented by the escaping alkaline (up to pH 12), H₂- and/or CH₄-rich, Ca-rich, but Mg- and CO₂-poor fluids (e.g., Bruni et al., 2002; Cipolli et al., 2004; Fritz et al., 1992; Kelley et al., 2001; Sanchez-Murillo et al., 2014; Schwarzenbach, Lang, et al., 2013). Microbial communities are found within chimney structures of hydrothermal vent fields and as microbial mats and biofilms around vent sites (Brazelton et al., 2011; Lang & Brazelton, 2020). They have been inferred to thrive within the serpentinite basement rock (Alt & Shanks, 1998; Schwarzenbach, Gill, & Johnston, 2018) and have been identified in emanating vent fluids (Brazelton et al., 2006, 2017; Morrill et al., 2013; Zwicker et al., 2018). Notably, in continental systems, the availability of vitally important elements such as sodium and sulfate is very limited, and concentrations are significantly lower than in marine environments where these species are abundant in seawater, which may limit the habitability of continental serpentinization systems (Suzuki et al., 2013).

In this study, we investigate the opaque mineralogy of partly serpentinized harzburgites from the Chimaera seeps in Turkey. These rocks were initially partly serpentinized on the Jurassic ocean floor and currently are subject to extensive interaction with highly methane-rich fluids as documented by methane vents (Etiope et al., 2011). Microbial activity has been shown to be abundant around the methane-rich vents emanating from the ground, and methane-, nitrogen-, iron-, and hydrogen-oxidizing bacteria as well as archaea, and metal-resistant bacteria have been identified at these sites (Neubeck et al., 2017; Zwicker et al., 2018). Here, we use high-resolution microstructural and -chemical investigations to explore the impact of fluid chemistry, especially the methane-rich fluids, on sulfide stability, and its implication to supporting life in active serpentinization systems, with a particular focus on pentlandite decomposition and awaruite formation. Sulfur isotopes are used to determine the origin of the sulfur and to infer sulfur speciation during the hydrothermal evolution of these rocks. We show that methane vents induce disequilibrium and destabilization of previously formed sulfides releasing H₂S and Fe to the fluid, forming porosity, and providing an additional energy source for microorganisms within serpentinites.

2. Geological Setting and Sample Selection

For this study, variably serpentinized harzburgites and lherzolites were collected near the Chimaera seep, close to the town of Çıralı in the Antalya Province, Turkey (Figure 1). The natural gas seeps, also known as Yanartaş, meaning “flaming rock” in Turkish, have been active for at least 2000 years and gas is emitted from around 50 vents, issuing along faults and from fractures in the rock (Etiope et al., 2011). The ultramafic rocks are part of the Tekirova ophiolitic unit. This unit belongs to the Antalya accretionary complex, which is one of the Mesozoic Neotethyan ophiolitic complexes in the eastern Mediterranean, and an accretionary wedge obducted onto an autochthonous carbonate platform during the closing of the Neotethyan Ocean (Aldanmaz et al., 2009). The Tekirova ophiolite includes an almost intact section of oceanic lithosphere including partly serpentinized harzburgites, minor lherzolites, dunites and chromites, isotropic gabbros, and sheeted dikes (Bağcı et al., 2006). The Tekirova ophiolite formed in the southern Neotethys in the late Cretaceous likely along a mid-ocean ridge spreading center (Aldanmaz et al., 2009; Bağcı et al., 2006). Though both MOR type and later suprasubduction-type peridotites are preserved, the formation of the latter is likely associated with the closure of the ocean (Aldanmaz et al., 2009).

The gas seeps are mostly venting from ultramafic rocks near the contact of the Tekirova ophiolite and shallow water carbonate-dominated sediments of the Kemer zone (Zwicker et al., 2018). The gas seeps consist mainly of methane (~87 vol.%), hydrogen (~10 vol.%), and N₂, with CH₄ formation having been associated with a thermogenic and abiotic origin linked to ongoing serpentinization in the subsurface (Etiope et al., 2011), though a partially microbial origin cannot be excluded (Zwicker et al., 2018). Active fluid seeps have only been reported at one location and, most likely, they only escape periodically with the fluid being of meteoric origin (Meyer-Dombard et al., 2015). Very similar to other continental sites of active

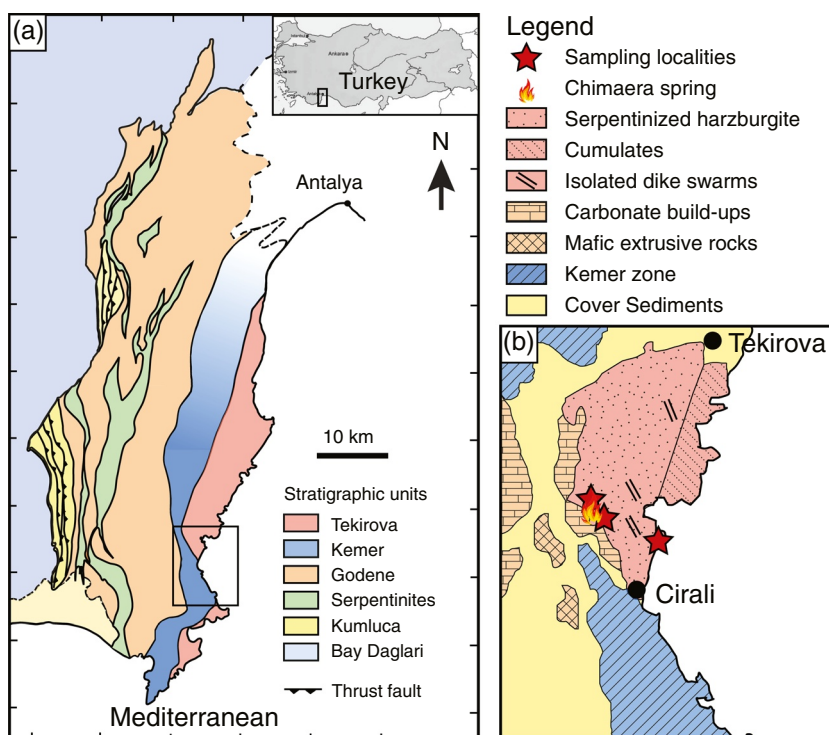


Figure 1. (a) Simplified tectonic map of the Antalya Complex in Turkey (modified after Robertson & Woodcock, 1980). (b) Detailed map (rectangle in [a]) of the lithologies near the Chimaera springs, with the sampling locations marked as red stars (modified after Bağcı et al., 2006).

serpentinization, a fluid pH of 11.95 was measured, with the fluid being very Ca^{2+} -rich—showing some of the highest concentrations yet detected in serpentinization systems—and Mg^{2+} and CO_2 -poor (Meyer-Dombard et al., 2015). Equilibrium formation temperatures for methane currently being emitted has recently been estimated based on clumped isotope signatures to $235^\circ\text{C} \pm 29^\circ\text{C}$ (Douglas et al., 2017), which is higher than previous estimates of $<50^\circ\text{C}$ – 100°C using the H_2 - CH_4 δD geothermometer (Etiope et al., 2011). Though a temperature of $<100^\circ\text{C}$ coincides with maximum temperatures at the base of the ophiolite and thus, maximum temperatures for current, continental fluid-peridotite interaction (Etiope et al., 2011).

Variably serpentinized harzburgites were collected from three outcrops and are shown in Figure 1. At all sampling sites, methane is venting from the ground, as previously described by Etiope et al. (2011).

3. Methods

For this study 19 rock samples were investigated (Table 1). For all samples, 30 μm thin sections and bulk rock powders were prepared. The mineralogy and petrology of the samples were examined on thin sections by transmitted and reflected light microscopy, and by electron microprobe analysis (EMPA), and scanning electron microscopy (SEM). EMP analyses were carried out on a JEOL 8200 Superprobe at the Freie Universität Berlin using 15 kV acceleration potential, a 20 nA current, and a 1 μm beam size using natural and synthetic reference material. High-resolution backscatter electron (BSE) images and element distribution maps were obtained with the Zeiss ATLAS software using a Zeiss Sigma 300 VP Field-Emission Scanning Electron Microscope equipped with two Bruker Quantax Xflash 6| 60 mm² SSD EDX Detectors for qualitative and quantitative element analysis also at the Freie Universität Berlin. Quantitative EDX maps were measured at 5 kV with a pixel size of 11 nm using the Ni-L α , Cu-L α , Fe-L α , S-K α , Mg-K α , and As-L α lines.

On one thin section site-specific, electron-transparent foils were prepared using a Thermo Fischer (former FEI) Helios G3 focused ion beam scanning electron microscope (FIB-SEM) to examine the micro-morphology of awaruite-pentlandite intergrowths. FIB-SEM foils were subsequently investigated using the

Table 1
Mineralogy of the Studied Ultramafic Samples From the Chimacra Hydrothermal Field

Sample name ^a	Lithology	Macroscopic description	Degree of serpentinization (in %)	Mineralogy ^b										Sulfide mineralogy ^c	
				Olivine	opx	cpx	Spinel	Serpentine	Chlorite	amph	Talc	Brucite	Carbonate		
CS-01	Carbonate-veined serpentinite	Covered with white serpentine, pervaded by serpentinite and calcite veins (mm sized)	>95	T	-	T	T	XX		T			O		rare ptl
CS-05 [†]	Serpentinite	Bastites visible macroscopically	No thin section												none detected
CS-06 [†]	Serpentinite	Mesh texture with bastites present	90–95	T	-	T	T	XX		O	T				ptl, aw
CS-07 [†]	Serpentinite		85–90	T	T	-	T	XX							none detected
CS-09 [†]	Serpentinite	Bastites visible macroscopically	No thin section												none detected
CS-10	Serpentinite	Mesh texture with bastites present	>95	T	T	T	T	XX		T					ptl, Cu-rich ptl (sm, sg)
CS-11 [†]	Carbonate-veined serpentinite breccia	Various sizes of the components, carbonate as veins and as aggregates	100	-	-	-		XX	O				O		none detected
CS-13 [†]	Serpentinite		80–85	O	O	-	T	XX							rare ptl, very rare native Cu
CS-14	Serpentinized harzburgite	Bastites visible	50–60	X	O		T	XX			T				ptl, Cu-rich ptl, sg, aw, rare native Cu
CS-16	Serpentinite	2 mm thick vein	70–75	O	O	T	T	XX			T				none detected
CS-17 [†]	Serpentinite	Carbonate-veined serpentinite	100	-	-	-	T	XX					O		none detected
CS-19 [†]	Serpentinite	Mesh texture with rare bastites present	100	-	-	-	T	XX			T		T		none detected
CS-20 [†]	Serpentinite	Covered with thick serpentinite veins	90	O	-	T	T	XX							none detected
CS-22	Serpentinite	Mesh texture with rare bastites present	100	-	-	-	T	XX	T	T					ptl, Co-ptl, hz, mil, aw, rare Cu-ptl (sg), rare gd
CS-25 [†]	Serpentinite	Mesh texture with rare bastites present	80–90	O	T	-	T	XX							none detected

Table 1
Continued

Sample name ^a	Lithology	Macroscopic description	Degree of serpentinization (in %)	Mineralogy ^b										
				Olivine	opx	cpx	Spinel	Serpentine	Chlorite	amph	Talc	Brucite	Carbonate	Sulfide mineralogy ^c
CS-26	Harzburgite	Thick 3–5 mm serpentine vein	30–40	XX	X	T	T	O	T					ptl, Cu-ptl, sg, sm, native Cu, cpy, cc, rare bn, aw
CS-30	Serpentinite	Fe-oxide very finely dispersed, mesh texture with bastites present	60–70	O	O	T	T	XX						ptl, Co-ptl, rare Cu-ptl, rare cpy, mil
CS-34	Serpentinite	Calcite veins	100				T	XX					T	ptl, Co-ptl, rare sm
CS-36 [†]	Harzburgite	Partly serpentinized, pyx more decomposed than ol	30–40	X	X	O	T	O						none detected

^aSamples marked with † did not yield detectable sulfur by bulk rock wet chemical sulfur extraction.

^bMineralogy: XX: ≥50%, X: 20%–50%, O: 5%–20%, T: <5% (determined by polarized light microscopy).

^cDetermined from EMPA: aw, awaruite; bn, bornite; cc, chalcocite; cpy, chalcopyrite; rd, rodlévszkite; ml, pentlandite; bz, heazlewoodite; mil, millerite; sm, samaniite; sg, suwakite.

^aSamples marked with † did not yield detectable sulfur by bulk rock wet chemical sulfur extraction.

^bMineralogy: XX: ≥50%, X: 20%–50%, O: 5%–20%, T: <5% (determined by polarized light microscopy).

^cDetermined from EMPA: aw, awaruite; bn, bornite; cc, chalcocite; cpy, chalcopyrite; gd, godlevskite; ptl, pentlandite; hz, heazlewoodite; mil, millerite; sm, samaniite; sg, sugakiite.

scanning mode of a Thermo Fischer (former FEI) Talos 200FX transmission electron microscope (TEM) operating at 200 kV and equipped with four energy-dispersive X-ray (EDX) detectors. EDX maps were collected and analyzed using the Bruker Esprit 2.1 software. All FIB-SEM and TEM investigations were carried out at the Utrecht University electron microscopy center.

For bulk rock sulfur isotope compositions and sulfur contents powders were prepared from all studied samples. First, the outermost 1–2 cm of the rock samples was cut away to remove contamination from weathering, then they were crushed with a hammer and finally powdered in an agate mill. Bulk rock sulfur was extracted as acid volatile sulfide (AVS, representing the monosulfide fraction), chromium reducible sulfide (CRS, representing the disulfide fraction), and sulfate by reaction of 20–30 g of bulk rock powder with 6M HCl and a CrCl₂-solution under N₂ atmosphere following a modified version of the methods described by Canfield et al. (1986) and Tuttle et al. (1986) (for details see Liebmann et al., 2018). AVS and CRS fractions were obtained as Ag₂S and the sulfate fraction as BaSO₄ precipitates. Precipitates were analyzed for their ³⁴S/³²S ratios on a Thermo Fisher Scientific MAT 253 mass spectrometer combined with an Eurovector elemental analyzer from HEKAtech by combustion to SO₂ gas. The international sulfide (Ag₂S) standards IAEA-S1, IAEA-S2, and IAEA-S3, the sulfate (BaSO₄) standards NBS-127, IAEA-SO₅, and IAEA-SO₆, and an in-house sulfate (K₂SO₄) standard were used as reference materials. Sulfur isotope compositions are reported in the conventional delta-notation (δ³⁴S) and reported against V-CDT. Analytical reproducibility of the analyses of the standards is better than ±0.12‰ for sulfides and ±0.26‰ for sulfates. The measurement error on S contents is typically better than 5%. For individual samples the error can be higher due to either sample heterogeneity and/or very low sulfide and sulfate concentrations, and was constrained from duplicate sample extractions and sample analyses, and is given in Table 2.

4. Results

4.1. Mineralogy

The studied samples are highly serpentinized clinopyroxene-bearing harzburgites with variable degrees of serpentinization (degree to which primary minerals are replaced by serpentine ± brucite ± talc) from ~30% to 100% (Table 1). In general, orthopyroxene is more extensively serpentinized compared to olivine. Most samples show a typical mesh texture where serpentine progressively replaces olivine, and bastites forming as orthopyroxene is progressively replaced by serpentine. Locally, chlorite, talc, and amphibole occur either as veins or replacing bastites. In a few samples, brucite occurs as veins or as aggregates in the serpentine groundmass. All samples contain Cr-rich spinel. Fine-grained iron oxides and iron hydroxides locally replace serpentine in the groundmass leading to a brown to reddish, variably oxidized groundmass. In addition, some entirely serpentinized peridotites are cut by carbonate veins and some samples are carbonate-veined serpentinite breccias.

Table 2
Bulk Rock Sulfur Isotope Compositions and Sulfur Contents

Sample name	S Content AVS		S Content CRS		Total sulfide ^a		S Content sulfate		Total S content ^b		SO ₄ /total S		δ ³⁴ S AVS		δ ³⁴ S CRS		δ ³⁴ S sulphate	
	(μg/g)	Error	(μg/g)	Error	(μg/g)	Error	(μg/g)	Error	(μg/g)	Error	Error	S	(%, V-CDT)	Error	(%, V-CDT)	Error	(%, V-CDT)	Error
CS-1	6,972	188	<10.d.		6,972	349	6,306	315	13,278	664	0.475	22.34	0.12	n.d.			20.71	0.26
CS-10	15	1	21	2	35	12	82	4	117	46	0.698	0.82	0.12	-0.64		3.16	13.27	0.26
CS-14	499	45	44	2	543	14	1,694	495	2,237	482	0.757	22.07	0.12	19.36	0.12	19.06	0.26	0.26
CS-16	45	6	47	23	92	29	106	5	198	46	0.536	2.38	1.10	2.06	0.64	13.42	0.29	0.29
CS-22	<10.d.		<10.d.		<10.d.		335	25	335	17	1.000	n.d.		n.d.		19.69	0.31	0.31
CS-26	13	1	246	12	260	13	430	193	690	35	0.624	1.17	0.12	0.22	0.12	16.62	2.30	2.30
CS-30	5	5	17	1	22	8	70	3	92	41	0.758	-0.11	0.12	-0.27	0.12	14.28	1.04	1.04
CS-34	8	1	186	9	194	10	489	64	682	34	0.716	12.18	0.12	9.44	0.12	15.81	1.20	1.20

^aTotal sulfide = AVS + CRS.

^bTotal sulfur content = AVS + CRS + sulfate.

Abbreviations: AVS, acid volatile sulfide; CRS, chromium reducible sulfide.

4.2. Sulfide Mineralogy and Chemistry

The opaque phases are comprised, apart from magnetite and fine-grained Fe-oxides/hydroxides, of sulfides, native metals, and metal alloys of manifold compositions. These include pentlandite [(Fe,Ni)₉S₈], Co-pentlandite [(Co,Fe,Ni)₉S₈], Cu-rich pentlandite (sugakiite [Cu(Fe,Ni)₈S₈] and samaniite [Cu₂(Fe,Ni)₇S₈]), heazlewoodite [Ni₃S₂], millerite [NiS], chalcocite [Cu₂S], native copper and awaruite (Ni_{2.3}Fe) (Figure 2, Tables 1 and S1). While in some samples no sulfide minerals, native copper, or awaruite could be detected, awaruite was found in samples of highly variable degree of serpentinization, from around 30% to around 90%–95%. Accordingly, there is no correlation between sulfide, alloy, or native metal mineralogy and either degree of serpentinization or silicate mineralogy.

In almost all samples investigated here, the sulfides and metals occur within the serpentine groundmass, that is, they are surrounded by serpentine. In all samples, pentlandite is the dominant sulfide mineral. Pentlandite is in most samples highly decomposed (Figures 3 and 4) and often intergrown with other mineral phases such as awaruite, magnetite, Cu-rich pentlandite (up to a composition of samaniite and sugakiite), chalcocite and/or native copper, or in one sample with millerite and heazlewoodite.

Pentlandite has a highly variable composition ranging (in the case of Cu-free pentlandite) from Fe contents up to 42.7 wt.% to Ni contents up to 55.7 wt.%, and up to 67 wt.% in the case of the Ni-rich godlevskite end member [Ni₈FeS₈] (Figure 2a). In most samples, Co contents in pentlandite are below 4 wt.%, except one sample (CS22) containing pentlandite with up to 14.5 wt.% Co. Heazlewoodite contains up to 3.4 wt.% Fe and millerite up to 1.9 wt.% Fe. For both minerals, Cu, Co, Zn, and As concentrations are below the detection limit. Heazlewoodite and millerite have only been detected intergrown with decomposing pentlandite, but not as single grains.

Cu-bearing sulfides include sugakiite and samaniite with up to 17 wt.% Cu that substitutes for Ni (16.0–39.3 wt.%) or Fe (17.8–40.7 wt.%) (Figure 2b). The Co content of these sulfides is typically below 1 wt.%. Chalcocite is very rare and contains 3.4 to 4.4 wt.% Fe. It was only detected intergrown with Cu-bearing pentlandite where Cu-rich, parallel exsolutions, and highly decomposed pentlandite occur (Figure 3c). Accordingly, spot analysis of the exsolved domains yields mixed analyses due to mineral intergrowth on the submicrometer scale (Figure 2). Similarly, in a few samples, Cu-rich sulfide minerals were detected, which, however, could not be classified due to their small grain sizes and their being intergrown with the pentlandite (Figures 3a–3d). Native copper could only be quantified by EMPA in sample CS26, though in several samples submicrometer-sized veins of native copper, formed within the center of serpentine veins, could be identified by EDX mapping (Figures 3d and 3e).

4.3. Awaruite Microstructure

The Fe-Ni alloy awaruite occurs exclusively next to or intergrown with pentlandite (Figures 3a and 4) and can be categorized into three distinct growth morphologies and assemblages: (i) awaruite intergrown with pentlandite as micrometer-scale dense veinlets or rims (e.g., Figures 4b and 4e, see also suppl. material Figure S2), (ii) as tens of nanometers thick platelets lacking magnetite (e.g., Figures 4e and 4f), or (iii) in a few samples as micrometer-scale vein-like features with magnetite, and/or native copper (Figure 3e). The dense awaruite veinlets or rims (i and iii) are up to 5 μm thick and represent a gen-

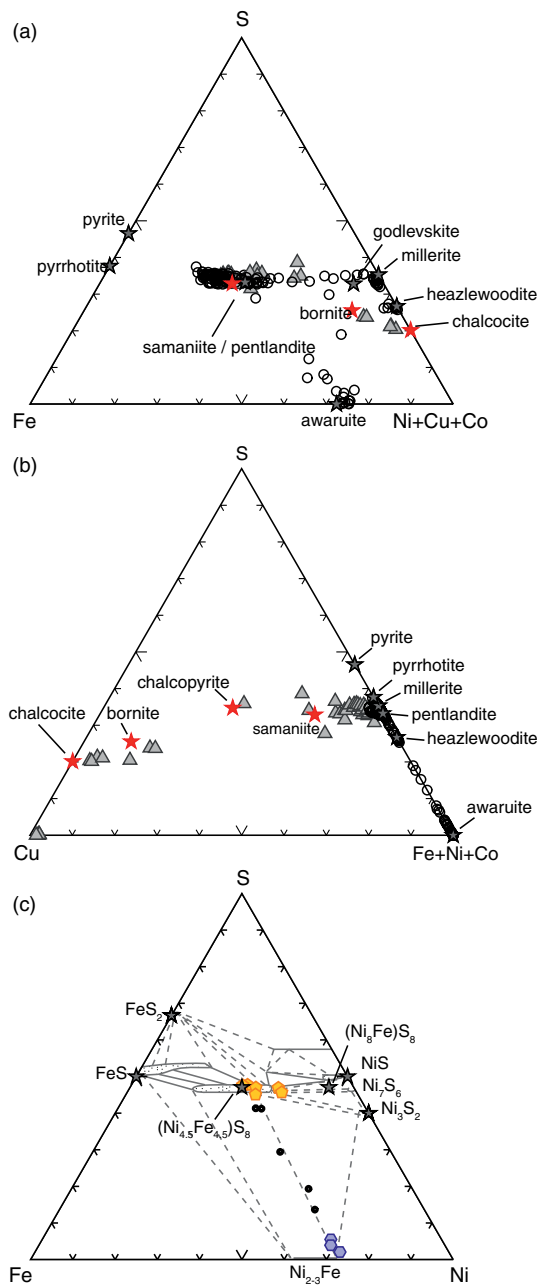


Figure 2. Ternary diagrams of (a) Fe-S-(Ni + Cu + Co) and (b) Cu-S-(Fe + Ni + Co) showing the range of chemical compositions detected in the studied samples (in wt.%). Gray triangles represent analyses containing >3 wt.% Cu, circles represent analyses containing <3 wt.% Cu. Note, numerous analyses represent mixed analyses due to mineral intergrowth at the submicrometer-scale. (c) Pentlandite-awaruite pairs of grain CS06_R71 with the stability fields in the S-Fe-Ni space for 230°C redrawn from Misra and Fleet (1973) (in atom%). Yellow pentagons = pentlandite, blue hexagons = awaruite, black circles = mixed pentlandite-awaruite analyses. Red stars represent the stoichiometric composition of Cu-bearing sulfides, black stars represent stoichiometric compositions of Fe- and Ni-sulfides and metals.

eration of awaruite formation that in some grains follows the octahedral parting planes of pentlandite (Figure 4a). TEM bright-field and HAADF images show that the awaruite_i rims consist of columnar single crystals oriented with their long axis normal to the parent pentlandite grain (aw_i in Figures 5g and 5h). A serpentine-filled submicrometer gap locally exists between the pentlandite parent and awaruite product (Figure 5). The composition of the nonporous awaruite_i rims ranges from Ni contents of 72.5–76.6 wt.% and Fe contents of 23.7–26.1 wt.% correspondings to a composition of Ni_{2.71–2.88}Fe. Co contents are <1wt.% and other metal concentrations are below the detection limit. Often, awaruite replaces pentlandite with the crystal shape of the educt remaining visible. Thus, we interpret this as a pseudomorphic replacement reaction. This is particularly evident where nm-scale platelets of awaruite_{ii} formed. This awaruite forms skeletal aggregates of ~40–70 nm thick platelets that commonly intersect at an angle of ~90° (aw_{ii} in Figures 4e and 5g, 5h). TEM imaging and EDX mapping show that this awaruite is intergrown with serpentine, occasionally with terminal sector-shaped morphologies (Figure 5). The replacement front between platy awaruite_{ii} and pentlandite is clearly also oriented parallel to subparallel to the octahedral parting planes {111} of pentlandite (Figures 4 and 5). However, a specific relationship between the crystallographic orientations of parent and product awaruite platelets could not be established based on SEM and TEM imaging. Serpentine-filled bands separate the matching surfaces of both awaruite generations (i and ii) and the pentlandite parent, suggesting a later breakup of awaruite-pentlandite interfaces.

4.4. Sulfur Isotope Composition

Bulk rock sulfur isotope compositions and contents are highly variable and reach in one sample up to 1.33 wt.% S in the bulk rock total sulfur content (Table 2, Figure 6). However, most samples yielded no detectable sulfide nor sulfate by wet chemical extraction. In samples with detectable sulfur, sulfate is typically the dominant sulfur phase (SO₄/total sulfur = 0.475 to 1.000) with sulfate contents of 70–6,306 μg/g, though mostly below 490 μg/g. AVS contents are typically between 5 and 499 μg/g, except for one sample with 6,972 μg/g AVS, and chromium reducible sulfide (CRS) contents are between 17 and 246 μg/g. While δ³⁴S values of sulfate have a relatively narrow range of 13.3–20.7‰, δ³⁴S values of AVS and CRS have a larger range of –0.1‰ to +22.3‰ and –0.6 to +19.4‰, respectively (Figures 6a and 6b). In general, the sulfide content determined from powdered samples agrees well with the sulfide abundance observed in thin sections, with a few exceptions that suggest sample heterogeneity in terms of sulfide mineral occurrence (e.g., sample CS-1) as reflected by slightly larger errors (Table 2).

5. Discussion

5.1. Origin of Sulfide and Metal Mineral Phases

Primary, unaltered mantle rocks have sulfide mineralogy typically consisting of pentlandite, pyrrhotite, and rare chalcopyrite (e.g., Lorand, 1987; Lorand, 1989), with sulfur being present only in its reduced state (S^{2–}, S^{2–}). The distinction between primary and secondary sulfide

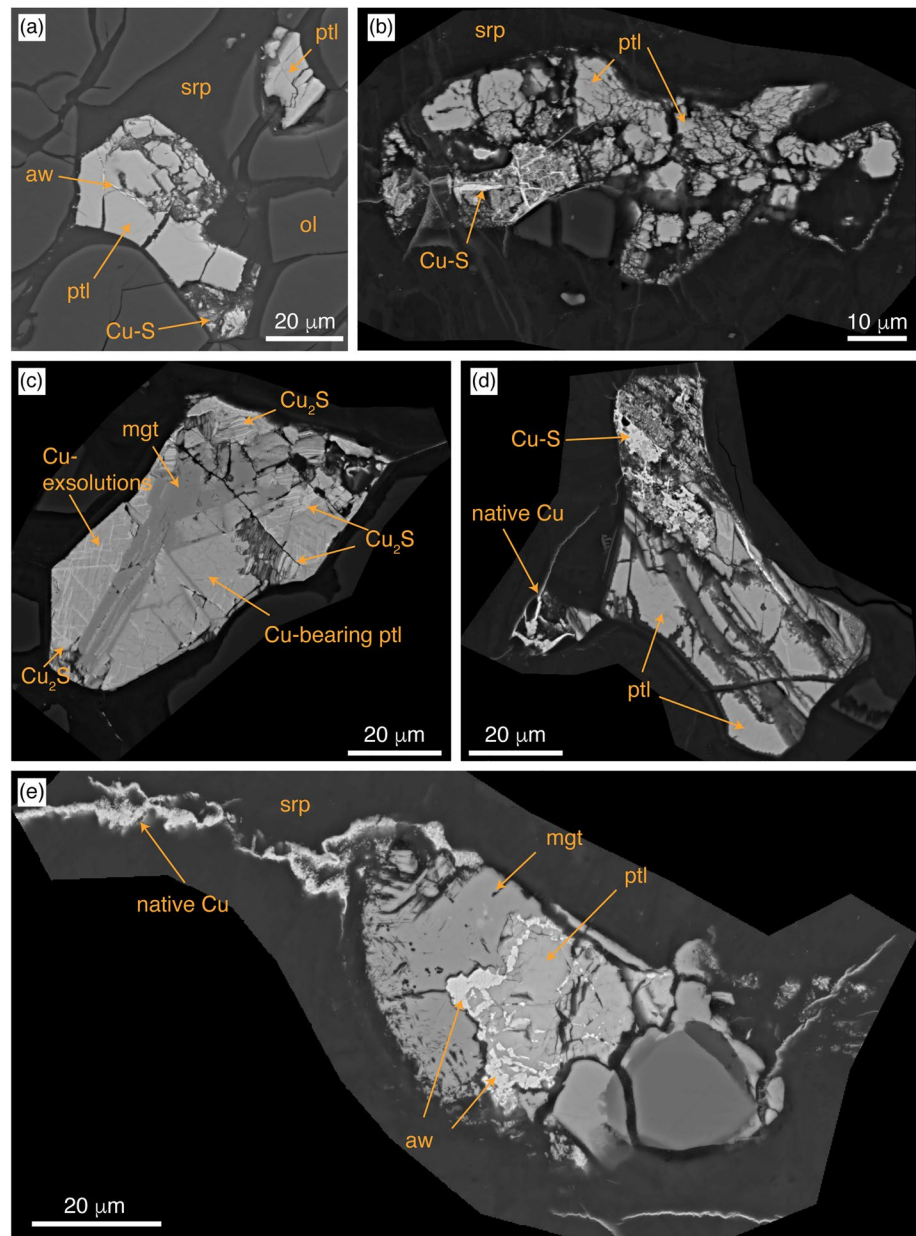


Figure 3. Backscattered electron (BSE) images of variably decomposed pentlandite grains partly altered to Cu-rich sulfide minerals (a–d), locally forming native copper mostly as vein-like features in the serpentine groundmass or in the center of serpentine veins (e). (c) Variably Cu-bearing pentlandite with Cu-rich exsolutions and with pentlandite breaking down to form chalcocite (Cu_2S). (e) Pentlandite intergrown with awaruite and magnetite. aw, awaruite; ol, olivine; srp, serpentine; ptl, pentlandite; mgt, magnetite.

minerals can be based on mineralogical evidence (e.g., crystal shape, mineralogy), but is often challenging particularly with regards to pentlandite and pyrrhotite unless they occur as inclusions in primary minerals (e.g., olivine, spinel) (Lorand, 1987). A second and relatively reliable tool to determine the origin of the sulfur is to use sulfur isotope compositions as the average depleted mantle is estimated to have a narrow range in $\delta^{34}\text{S}_{\text{sulfide}}$ values of $0 \pm 1\%$ (Figure 6c) (Sakai et al., 1984; Shanks, Böhlke, & Seal, 1995).

Based on the $\delta^{34}\text{S}_{\text{sulfide}}$ values of the studied samples some pentlandite is most likely of depleted mantle origin as reflected by $\delta^{34}\text{S}$ values of -0.6% – 2.1% (Figure 6c). However, a range in $\delta^{34}\text{S}_{\text{sulfide}}$ values of up to

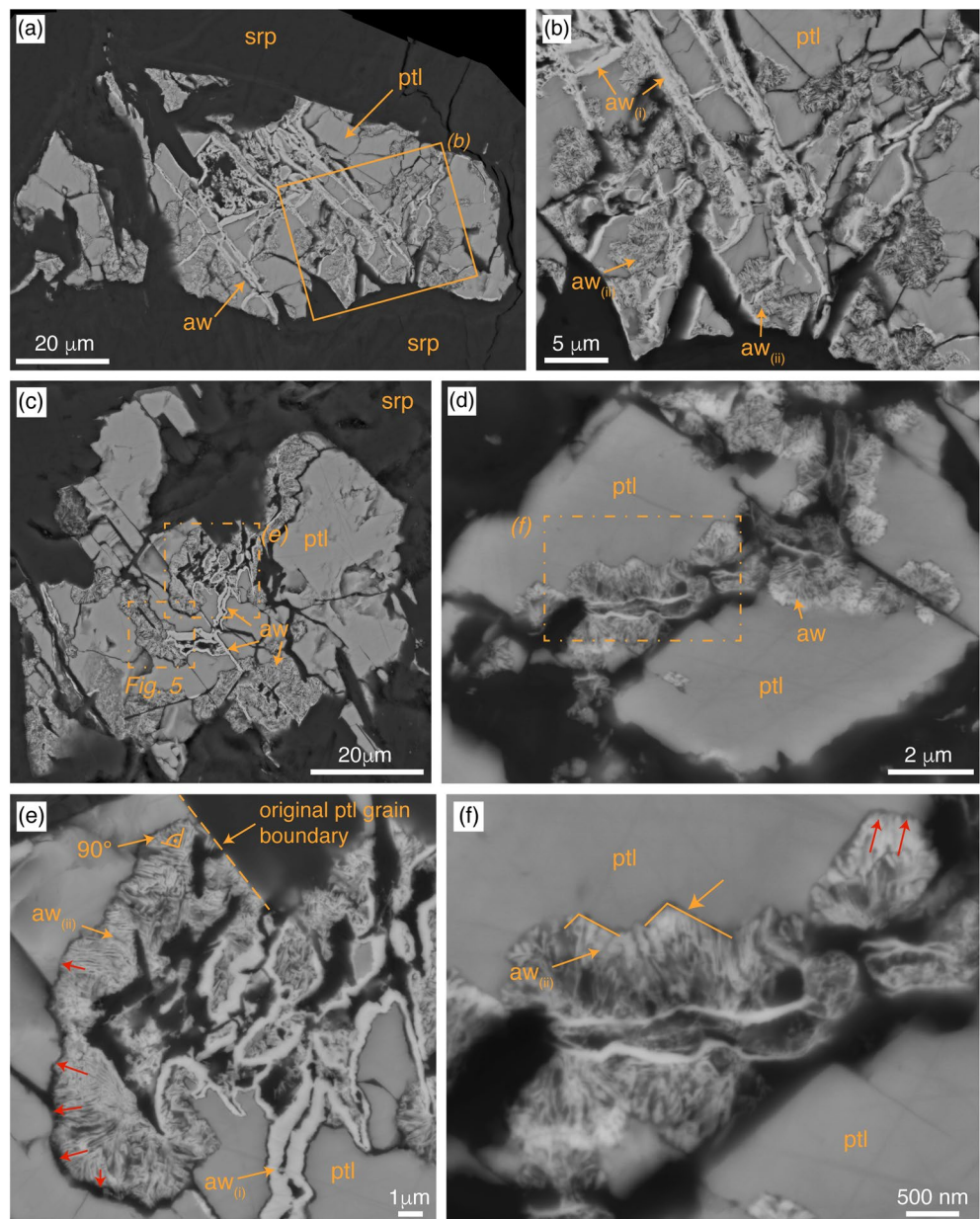


Figure 4. Backscattered electron (BSE) images of variably decomposed pentlandite with dense awaruite ($aw_{(i)}$) forming along orthogonal cleavage planes of the pentlandite (a–c) or locally cutting pentlandite as irregular veins (e). Awaruite ($aw_{(i)}$) forming nanometer thin platelets are highlighted in (e) with awaruite increasingly consuming pentlandite (red arrows) and replacing it pseudomorphically (original pentlandite grain boundary is indicated) with awaruite platelets often intersecting at an angle of 90° . Locally pentlandite is consumed along orthogonal cleavage planes forming awaruite platelets (f). (b, e, and f) are magnifications of areas shown in (a, c, and d), respectively. Abbreviations as in Figure 3.

+22.3‰ clearly documents at least in part a secondary origin of the sulfide, which is further supported by a dominance of oxidized sulfur in the bulk rock (Figure 6b), both documenting introduction of reduced and oxidized sulfur most likely associated with serpentinization of the peridotite. Furthermore, a secondary origin of the sulfide and metal mineral, as well as extensive water-rock interaction and changing fluid redox conditions associated with peridotite alteration, is evidenced by the abundance of strongly decomposed pentlandite and pentlandite intergrown with diverse Cu-bearing sulfides, metals, or metal alloys (Figures 3 and 4).

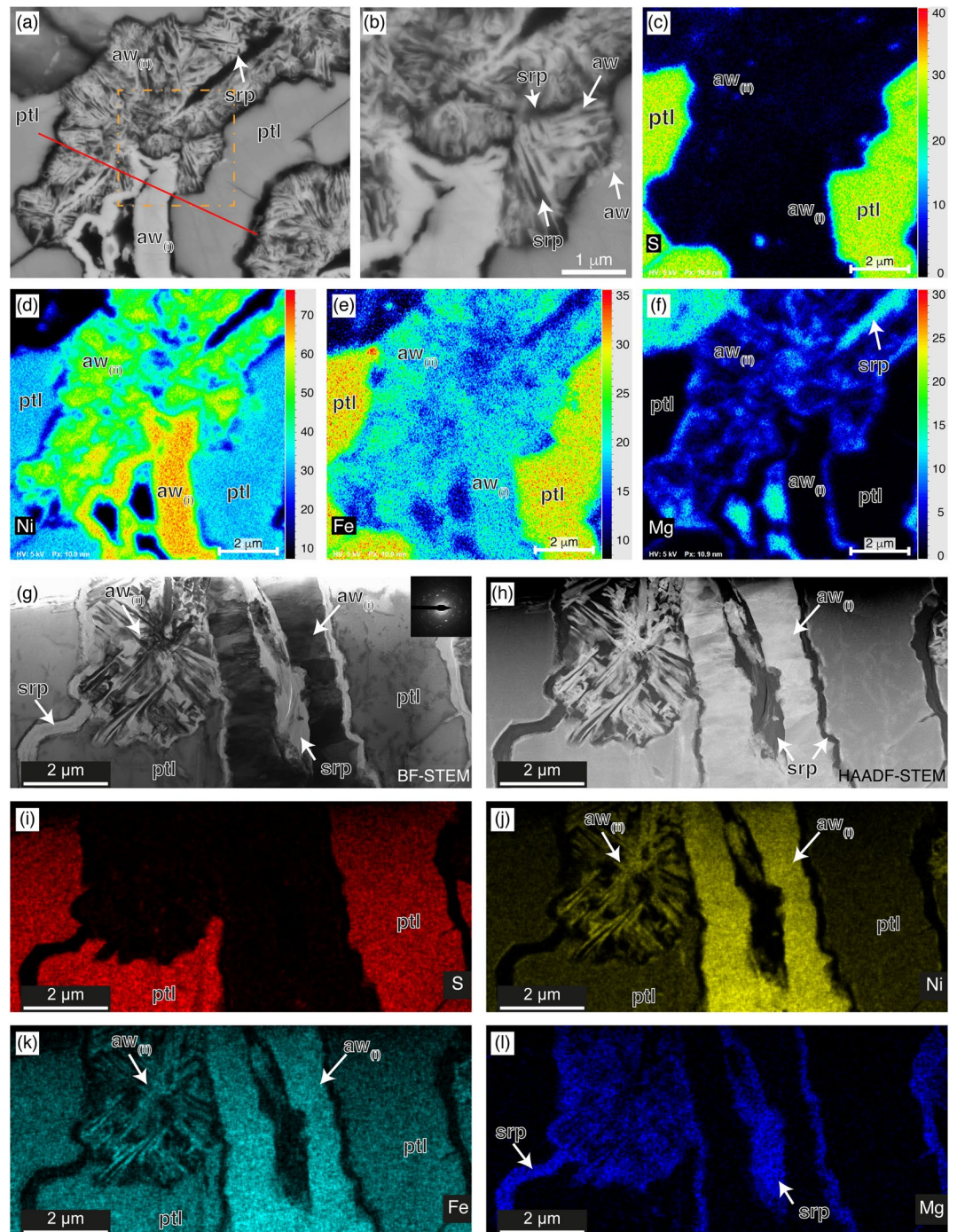
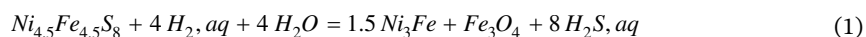


Figure 5. (a–f) BSE images and quantitative EDX maps measured with a pixel size of 11 nm (see area shown in Figure 4c) for S, Ni, Fe, Mg, of pentlandite (ptl) replaced by two generations of awaruite: dense awaruite (aw_(i)) and platelet aggregates (aw_(ii)). Panel (b) is a magnification of (a) (dashed-orange rectangle) and represents the mapped area in (c–f). (g) Bright-field (BF-STEM), and (h) High-angle annular dark-field scanning transmission electron microscopy (HAADF-STEM) image, as well as element mappings (i–l) of the same area (red line in (a) indicates the cut FIB-SEM-section). Columnar aw_(i) crystals are oriented with their long axis normal to the parent pentlandite surface and separated from this substrate by a thin serpentine layer. Later aw_(ii) platelets are up to 2 μm long single crystals and 70 nm thick. They intersect at an angle of ~90° and are intergrown with late serpentine. BSE, backscattered electron; EDX, energy dispersive X-rays.

Interestingly, no secondary sulfides other than pentlandite were detected as single mineral grains. In other words, heazlewoodite, millerite, and Cu-bearing sulfide minerals have been exclusively detected intergrown with pentlandite. This indicates that pentlandite (and possibly pyrrhotite and chalcopyrite) decomposition and alteration were a major mechanism for secondary sulfide formation. In oceanic serpentinites and serpentinized peridotites, precipitation of sulfide minerals associated with microbial sulfate reduction or introduction of high-temperature S-bearing fluid result in either massif sulfide deposits, euhedral to fracture filling sulfides, finely disseminated sulfides (<1 μm) in the serpentine mesh texture, or in rare cases framboidal sulfide minerals, with their mineralogy reflecting prevalent $f\text{O}_2$, $f\text{H}_2$, and $a(\text{H}_2\text{S})$ conditions (Alt et al., 2007; Delacour et al., 2008; Marques et al., 2007; Schwarzenbach et al., 2012). This implies that only rare secondary sulfide minerals formed in the studied samples during hydrothermal alteration and/or that subsequent fluid-rock interaction destabilized these mineral phases, that is, resulted in their decomposition and partial dissolution if, example, $a(\text{H}_2\text{S})$ decreased as shown by thermodynamic modeling (Foustoukos et al., 2015; Frost, 1985; Klein & Bach, 2009). A change in sulfide/metal mineralogy has previously been shown particularly associated with the formation of awaruite, which forms due to the high H_2 concentrations released during serpentinization that cause desulfurization of pentlandite according to the reaction (Klein & Bach, 2009; Schwarzenbach et al., 2014):



This reaction has been inferred from dense awaruite as reaction rims on or veinlets within pentlandite in, example, serpentinites from ODP Leg 209 along the Mid-Atlantic Ridge (Alt et al., 2007; Klein & Bach, 2009), peridotites from the Santa Elena ophiolite (Schwarzenbach et al., 2014), or serpentinized dunites of the Muskox intrusion (Chamberlain et al., 1965).

Similarly, the micromorphology of the Cu-bearing sulfides in the partly serpentinized harzburgites studied here points to a secondary origin. Copper-bearing sulfide minerals and native copper have been described in variably serpentinized peridotites from the Santa Elena ophiolite in Costa Rica. These have been attributed to a mostly secondary origin and formation associated with high-temperature ($\sim 350^\circ\text{C}$) fluids that contain small amounts of copper within a mid-ocean ridge environment (Schwarzenbach et al., 2016). The mineral precipitation took place at very low water-rock ratios, effectively leading to positive $\delta^{34}\text{S}_{\text{sulfide}}$ values due to fluid evolution toward a closed system (Figure 6c) (Schwarzenbach et al., 2014, 2016). The sulfur isotope composition of the here studied rocks coincides with such a scenario; the $\delta^{34}\text{S}_{\text{sulfide}}$ values of the Chimaera samples mostly overlap with the isotope composition of the Santa Elena ophiolite suggesting that (Cretaceous) seawater-derived sulfate was abiogenically reduced to form sulfide and that sulfide was added by the hydrothermal fluids in a seafloor setting (Figure 6c). (Note, Santa Elena and Chimaera peridotites were both serpentinized in the Cretaceous where $\delta^{34}\text{S}_{\text{seawater-sulfate}}$ values were around 16–19‰; Present et al. [2020]). However, the abundance of vein-like native copper forming in the center of serpentine veins (see Figure 3e) indicates that native copper formed during a later stage of fluid-rock interaction. Copper is a relatively reactive element and precipitates in its native state at highly variable $f\text{O}_2$, but low $f\text{S}_2$ conditions (Schwarzenbach, Gazel, & Caddick, 2014). Native copper has been described in hydrothermal systems that formed by supergene alteration and oxidation of sulfide deposits by ambient seawater in the TAG (Trans-Atlantic Geotravers) field (Hannington et al., 1988) or during low-temperature, epigenetic hydrothermal alteration of comparatively Cu-rich basalts (e.g., Bing-Quan et al., 2007; Pinto et al., 2011).

Hence, based on the sulfur isotope compositions, we infer that hydrothermal alteration of the peridotites associated with seafloor spreading was accompanied by localized high-temperature fluids that introduced sulfide and trace amounts of copper to form copper-bearing sulfides similar to the process observed in the Santa Elena ophiolite (Schwarzenbach et al., 2014). This was associated with thermochemical sulfate reduction with sulfur isotope fractionation by closed system fluid evolution resulting in $\delta^{34}\text{S}_{\text{sulfide}}$ values up to 22.3‰ (Table 2). A seafloor origin of the pentlandite is further corroborated, as thermochemical sulfate reduction is not proceeding efficiently at $<250^\circ\text{C}$ (Shanks et al., 1981) and hence is not proceeding at the low temperatures currently prevailing in the subsurface of the Chimaera hydrothermal field ($<100^\circ\text{C}$) (Etiope et al., 2011). In contrast, the textural relations of the native copper veinlets within the center of serpentine veins suggest these formed after ophiolite emplacement, most likely by subsequent alteration of Cu-sulfides related to meteoric fluid circulation.

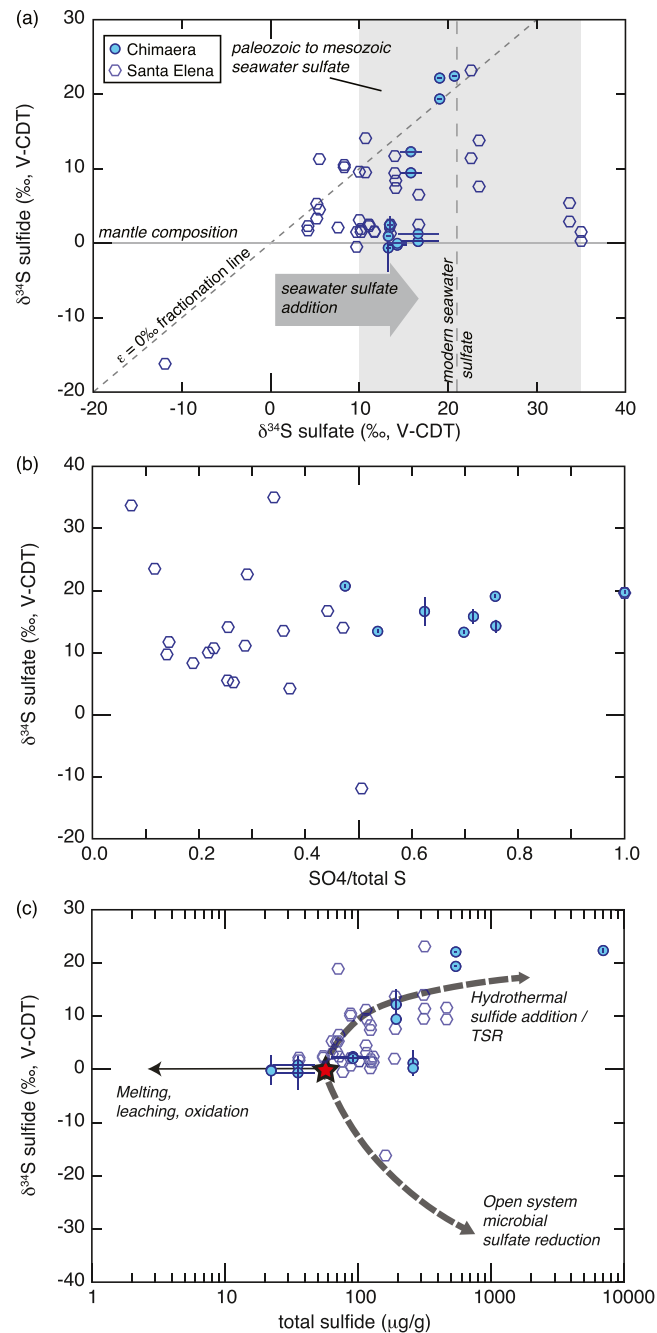


Figure 6. Bulk rock sulfur isotope compositions of the studied samples compared to peridotites from the Santa Elena ophiolite in Costa Rica (Schwarzenbach et al., 2016) (only samples that yielded detectable sulfur are shown). (a) $\delta^{34}\text{S}$ of sulfate against $\delta^{34}\text{S}$ of the sulfide fractions (AVS and CRS) indicating later addition of sulfate either from modern or an ancient seawater sulfate reservoir. The light gray area indicates $\delta^{34}\text{S}$ composition of Paleozoic to Mesozoic seawater (after Kampschulte & Strauss, 2004; Present et al., 2020). (b) Most samples from the Chimaera hydrothermal system are dominated by sulfate over sulfide and have a relatively narrow range in $\delta^{34}\text{S}_{\text{sulfate}}$ values. (c) $\delta^{34}\text{S}$ of AVS and CRS extracts shown against total sulfide contents. Chimaera samples have sulfide compositions very similar to those found in the Santa Elena peridotites that have been associated with thermochemical sulfate reduction at increasingly limited sulfate input, that is, low water-rock ratios. Processes indicated by the arrows and average depleted mantle composition (red star) after Alt et al. (2007). AVS, acid volatile sulfide; CRS, chromium reducible sulfide.

5.2. Mechanisms Resulting in Awaruite Formation

The two generations of awaruite micromorphologies (columnar awaruite_i vs. up to 2 μm long, 40–70 nm thin awaruite_{ii} single crystals, see Figure 4) strongly indicate formation during contrasting episodes of hydrothermal circulation, that is, different replacement episodes resulting from differing reaction kinetics imposed by changing temperatures and/or fluid properties, as discussed in the following. The chemical composition of the μm -scale vein-like awaruite-pentlandite pairs indicates formation temperatures of around 230°C using the phase relations in the Fe-S-Ni system from Misra and Fleet (1973) (Figure 2c). This infers formation during ocean floor alteration rather than low-temperature interaction with meteoric fluids and coincides with previous observations of dense awaruite rims or veinlets intergrown with magnetite and pentlandite from oceanic settings (Alt et al., 2007; Klein & Bach, 2009). Based on the micromorphologies it is likely that most of the denser awaruite_i that either forms veinlets, rims, or forms along the octahedral parting planes of pentlandite is associated with this stage of water-rock interaction. Interestingly, this temperature overlaps with temperatures constrained from clumped isotope thermometry for abiogenic methane formation of $235^\circ\text{C} \pm 29^\circ\text{C}$ (Douglas et al., 2017). This may suggest a concurrent formation of methane and the early awaruite generation in an ocean floor setting. However, these temperatures can only be constrained where awaruite forms up to micrometer-thick intergrowths with pentlandite. The small size of the later platy awaruite_{ii} does not allow quantification of the exact chemical composition and hence no precipitation temperatures can be constrained.

Overall, the uniform orientation of columnar awaruite_i single crystals in rims (Figures 5g and 5h) and particularly the replacement front between nanometer-scale awaruite_{ii} platelets and pentlandite octahedral parting planes (Figure 4e) evidence a coupled dissolution-precipitation process. Such a mineral replacement mechanism proceeds when fluid comes into contact with a solid phase with which it is not in equilibrium (Putnis, 2009). A coupled dissolution-precipitation process is characterized by the preservation of the morphology of the parent phase (in our case pentlandite) (Figures 4a and 4c), a distinct replacement front (Figure 4e), and formation of porosity, which allows continuous transport of fluid to the parent phase and reaction of fluid with the parent phase to produce the reaction product (in our case awaruite) (Plümper et al., 2017; Putnis, 2009; Putnis & Putnis, 2007).

We infer that the first stage of fluid-rock interaction produced columnar (dense) awaruite_i on dissolving pentlandite and took place within an ocean floor setting induced by H_2 production during ongoing serpentinization at $>200^\circ\text{C}$. Based on the distinctly different awaruite morphologies we infer that the second stage pentlandite decomposition to awaruite_{ii} platelets was most likely the effect of higher disequilibrium conditions with the fluid phase caused by changes in fluid chemistry and/or temperature. These conditions resulted in the formation of up to 2 μm long and 40–70 nanometer thin awaruite_{ii} single crystals (Figures 5g and 5h). The morphology of the serpentine crystals in cracks and in the pore space between awaruite_{ii} platelets suggests serpentine either formed during pentlandite replacement or after it fills the pore space, documenting that this stage of awaruite formation was also associated with serpentinization of the peridotite. Disequilibrium could be caused by two different factors; First, at decreasing $a(\text{H}_2\text{S})$ pentlandite becomes thermodynamically unstable (e.g., Frost, 1985; Klein & Bach, 2009), suggesting that highly S-undersaturated fluid conditions effectively result in decomposition of pentlandite to form awaruite (see Equation 1). While seawater has sulfate concentrations of around 2,650 mg/L (28 mM), SO_4^{2-} concentrations in the Chimaera springs are on the order of 8 mg/L (Meyer-Dombard et al., 2015). Similarly, H_2S concentrations are likely exceedingly low as well in the Chimaera springs (though they have not been reported yet for these springs), as is also typical in other continental serpentinization systems (Sabuda et al., 2020). Such low $f\text{S}_2$ ($a(\text{H}_2\text{S})$) conditions could induce pentlandite decomposition and awaruite formation releasing H_2S to the fluid as a consequence (Klein & Bach, 2009). Second, the Chimaera vents comprise $\sim 87\text{ vol}\%$ CH_4 and $\sim 10\text{ vol}\%$ H_2 (Etioppe et al., 2011). The formation of awaruite due to high $f\text{H}_2$ has been constrained thermodynamically (Klein & Bach, 2009) and may be used as a proxy for the sulfide stabilities. Since both CH_4 and H_2 act as strong reducing agents, it is most likely that both species have the same redox potential stabilizing metal alloys, that is, destabilizing pentlandite. The lack of magnetite in the pentlandite-awaruite intergrowths studied here, which is usually found together with pentlandite-awaruite assemblages (Klein & Bach, 2009), further suggests that magnetite was either not stable, that is, conditions were more reducing, temperatures were too low (Klein, Bach, Humphris, et al., 2014), and/or that Fe^{3+} —typically taken up by magnetite—was

incorporated by another phase, such as serpentine. A similar process may also take place when awaruite precipitates as single grains in a serpentine matrix such as described in serpentinites from the Cache Creek terrain (Britten, 2017). In that case, awaruite forms during ongoing serpentinization at high fH_2 with Fe and Ni derived from olivine and pyroxene breakdown, whereas Fe^{3+} would be taken up by the surrounding serpentine. Most likely, in the Cache Creek samples the formation of awaruite crystals took place close to equilibrium enabling massive, well-developed crystals, which is in contrast to the effectively more dendritic awaruite_{ii} observed in our study that is typical for formation far from equilibrium (Sunagawa, 2005).

This overall indicates that the awaruite platelets formed as a result of the interaction of the methane-rich, sulfur-poor fluids during continental serpentinization, possibly in the presence of a free gas phase and, hence, at a later stage than some of the denser awaruite. However, in a few samples, we cannot exclude that some of the denser awaruite could have formed also during late-stage interaction associated with continental serpentinization. This is especially the case where the awaruite_{ii} platelets merge into denser, a few 100-nm-thin awaruite_i veinlets (e.g., Figures 4e and 5a). Importantly, the pore space had to be fluid-saturated as long as the reaction proceeded to allow for fluid flow toward the reaction interface and to allow for continuous pentlandite decomposition and awaruite formation, whereas in the absence of available fluid the reaction would have stopped. This has been demonstrated previously by for example, Putnis (2009). Platy awaruite_{ii} formation was most likely facilitated as the rock had already been partly serpentinized, which provided additional fluid pathways due to the presence of nanometer-scale pore space within the serpentinite groundmass (Tutolo et al., 2016) rather than the grains being enclosed within primary minerals.

Accordingly, our analytical results provide evidence that pentlandite is either of magmatic origin or formed during peridotite alteration along an oceanic spreading center. Based on the composition of pentlandite-awaruite pairs and the temperature constraints for thermochemical sulfate reduction discussed above, seafloor serpentinization would have taken place at a temperature range around 230°C–350°C induced by the introduction of Cretaceous seawater. As shown in many oceanic serpentinites this stage was associated with fluids of different origin (see e.g., Schwarzenbach et al., 2018) precipitating Cu-sulfides by high-T fluid influx and on the other hand producing awaruite by lower T (i.e., ~230°C) fluid circulation of highly reducing fluids. In particular, during this stage, stress-induced fracturing of the sulfide minerals caused parting along octahedral parting planes of the pentlandite (Figures 7a and 7b), whereas micrometer-thick awaruite_i rims composed of columnar single crystals formed along these fractures (Figure 7c), as the peridotite was undergoing serpentinization. A change toward highly S undersaturated and highly reducing (high fCH_4 and fH_2) conditions—most likely associated with interaction with meteoric water during continental serpentinization—caused further pentlandite breakdown and pseudomorphic replacement by nanometer-scale awaruite_{ii} platelet aggregates, while serpentine precipitated in the newly formed pore space.

Effectively, the replacement of pentlandite by the awaruite_i platelets leads to a considerable increase in pore space (though subsequently filled by serpentine) as well as a loss of Fe (the Ni/Fe ratio changes from ~0.8 in pentlandite to ~2.8 in awaruite) and H_2S . This H_2S loss is also evident in the widespread decomposition of sulfide minerals in most of the studied samples (e.g., Figure 2b). We infer that the very low $a(H_2S)$ in the meteoric fluids caused general sulfide mineral breakdown and the formation of Cu-rich sulfide minerals that are stable at highly variable fO_2 and fH_2 conditions (Schwarzenbach, Gazel, & Caddick, 2014). It is likely that within continental serpentinization environments redox conditions are highly variable and may range from highly oxidizing where fresh, oxygenated meteoric water enters the system to strongly reducing where the methane-hydrogen-rich fluids are circulating. This likely also explains the observed variety in opaque phases.

The loss of H_2S is also reflected in the low sulfide yields during wet chemical sulfur extraction, with sulfur contents below detection limit for most studied samples. Some of the sulfide minerals may have been oxidized to sulfate. Though the low sulfate contents of most samples and $\delta^{34}S_{sulfate}$ values of 13.2‰–20.7‰ rather point to the addition of seawater-derived sulfate because oxidative weathering of sulfide minerals is associated with an enrichment factor $\epsilon \approx 0\text{‰}$, which could not be observed here (Figure 6a) (Alt et al., 2007; Rye et al., 1992). Seawater sulfate could have been introduced by the methane-rich fluids. These have been inferred to circulate through the lower lying Upper Paleozoic to Lower Mesozoic shales that are the source rock of the methane seeps (Hosgörmöz, 2007). The $\delta^{34}S$ composition of seawater sulfate in the Paleozoic and Mesozoic varied between +10‰ and +35‰ (Kampschulte & Strauss, 2004; Present et al., 2020)

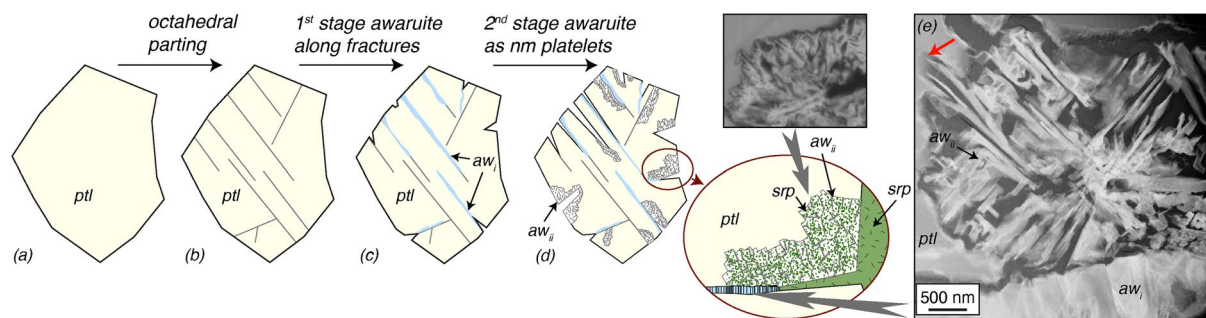


Figure 7. Schematic description of pentlandite decomposition and replacement by awaruite, with (b) initial octahedral parting, (c) awaruite replacing pentlandite along with octahedral fractures and locally in veins, and (d) awaruite platelets pseudomorphically replacing pentlandite associated with significant porosity increase, H_2S and Fe loss. The pore space is filled by serpentine either during or after final awaruite formation. (e) Columnar awaruite and nanometer-scaled awaruite platelets with a red arrow indicating pentlandite dissolution and awaruite precipitation.

and hence could have contributed trace amounts of sulfate to the rock (Figure 6a). The input of modern seawater-sulfate can, however, not be excluded. Overall, the sulfur geochemistry clearly points to multiple generations of sulfur cycling in the studied samples.

5.3. Implications for Microbial Activity

Previous studies have shown that microbial communities are found within ultramafic basement rocks, as documented by negative $\delta^{34}S$ signatures of serpentinites from the Iberian Margin, the Northern Apennine, and various drill core samples from the Mid-Atlantic Ridge (e.g., Alt et al., 2007; Alt & Shanks, 1998; Delacour et al., 2008; Schwarzenbach et al., 2018). In these rocks, evidence for microbial sulfate reduction can be traced to at least 150 m depths of the basement (Alt & Shanks, 1998). Similarly, sulfate reducers, sulfide oxidizers, and microbes using intermediate thiosulfate species have been detected within fluids of continental sites of serpentinization (e.g., Sabuda et al., 2020; Zwicker et al., 2018). While sulfate-reducing microbes may live within fractures and cracks, the occurrence of finely disseminated sulfide minerals with biogenic signatures also suggests that they possibly live within the pore space of serpentinites (Schwarzenbach et al., 2018). Tutolo et al. (2016) showed that the porosity of a peridotite can considerably increase as a result of the serpentinization reaction. Although in their case the pore space is most likely within the nanometer scale but has recently been shown to potentially play a pivotal role in the synthesis of abiotic carbon compounds (Nan et al., 2020). Alternatively, we suggest that low temperature water-rock interaction that causes destabilization of sulfide minerals, example, pentlandite-awaruite replacement (Figure 4) or pentlandite dissolution (Figure 3b), can result in considerable porosity that potentially provides a habitat for microbial communities. The increase of porosity effectively produced during pentlandite-awaruite replacement is on the order of 40%, with pores in the range of a few tens of nanometers between the platelets and larger pore space in the range of up to one micrometer in fractures of the sulfides (e.g., Figures 2d and 3e). Simultaneously, Fe, H_2S as well as other trace elements such as Co are released during sulfide decomposition. The porosity formed between the awaruite platelets and the extensive reactive mineral surface created by the replacement process is thereby key in allowing for continuous and coupled dissolution-reprecipitation to proceed and thus to continuously serve as an H_2S source for microbial life, for example, in adjacent fractures, whereby the pore space serves as ideal pathways for fluids to continuously react with the minerals.

At the Chimaera hydrothermal field, the presence of sulfate-reducing bacteria has been inferred based on biomarker studies and DNA extractions from surface rock samples (Neubeck et al., 2017; Zwicker et al., 2018). For Chimaera as well as other sites of active serpentinization, it has been suggested that sulfate reducing (and potentially sulfide oxidizing) microbes exist in microenvironments where active fluid-peridotite interaction provides niches for both sulfate-reducing bacteria but also methanogens, which are the more abundant species (Zwicker et al., 2018). Hence, we suggest that H_2S and Fe released by sulfide decomposition serve as energy sources for sulfide- and Fe oxidizing microbes at depth. Some H_2S may be transported toward shallower depths where mixing with oxygenated meteoric water takes place and sulfide is oxidized to sulfate serving as an energy source for sulfate reducers. In addition, sulfate leached from underlying

carbonate sequences and preserved as traces in the serpentinites may serve as an additional energy source for sulfate reducers.

6. Conclusions

Variably serpentinized peridotites from the methane-rich Chimaera hydrothermal field in Turkey have experienced multiple phases of fluid-rock interaction. Peridotite alteration by Cretaceous seawater along an ocean ridge spreading center took place at around 230°C–350°C and resulted in pentlandite precipitation associated with thermochemical sulfate reduction, likely at low water-rock ratios causing positive $\delta^{34}\text{S}_{\text{sulfide}}$ values as a result of isotope fractionation following closed system processes. This stage of water-rock interaction was associated with the introduction of high-temperature fluids that contributed small amounts of Cu. Within the same setting, dense polycrystalline awaruite_i rims formed along octahedral parting planes of pentlandite due to the highly reducing conditions imposed by ongoing serpentinization. The formation of awaruite generations at different fluid conditions is strongly supported by their different growth morphologies. We suggest that skeletal, nanometer-sized awaruite_{ii} platelets formed following the obduction of the ophiolite and interaction with meteoric water. At this stage of water-rock interaction, the fluids are rich in CH₄ and H₂, whereas a(H₂S) is very low. We infer that the very low a(H₂S) of the circulating meteoric fluids and the high CH₄ concentrations induced strong disequilibrium conditions particularly with respect to pentlandite, as well as other sulfide phases, and induce their destabilization. Due to the heterogeneous nature of these systems, redox conditions may be highly variable ranging from oxidizing where oxygenated meteoric water enters the system to highly reducing where the CH₄-H₂-rich fluids are channelized, but conditions are throughout sulfur-poor. These variations are reflected in the diverse opaque mineralogy from native copper, millerite, and heazlewoodite to the Fe-Ni alloy awaruite.

We infer that especially in these energy-limited systems the release of chemical species by mineral decomposition reactions induced by sulfur-undersaturated, meteoric fluids may be essential. In particular, the availability of S, Fe, and potentially other trace metals such as Co, and the formation of porosity that allows for fluid pathways and potentially serves as habitats for microbial communities may be key in supporting life within the basement of active serpentinization environments. Above all, these reactions may also be essential in supporting life on other water-bearing planets and planetary bodies, where water-peridotite interaction may take place in their crust or mantle.

Data Availability Statement

All datasets for this research are included in this study and its supplementary information files Table S1. In addition, all data are available in the Zenodo Repository, at <https://doi.org/10.5281/zenodo.4700157>.

Acknowledgments

The authors thank Alexander Schwarz and Sabine Meister for their help during analytical work. Benjamin Tutolo and Wolf-Achim Kahl are thanked for constructive comments and suggestions and Susanne Straub for editorial handling. Funding for this research was in parts provided by the Deutsche Forschungsgemeinschaft (DFG) grant SCHW 1889/4-1 to Esther Schwarzenbach. Oliver Plümper is supported by a European Research Council (ERC) starting grant “nanoEARTH” (852069). We acknowledge support by the German Research Foundation and the Open Access Publication Fund of the Freie Universität Berlin. Open Access funding enabled and organized by Projekt DEAL.

References

- Aldanmaz, E., Schmidt, M. W., Gourgaud, A., & Meisel, T. (2009). Mid-ocean ridge and supra-subduction geochemical signatures in spinel-peridotites from the Neotethyan ophiolites in SW Turkey: Implications for upper mantle melting processes. *Lithos*, 113, 691–708. <https://doi.org/10.1016/j.lithos.2009.03.010>
- Alt, J. C., & Shanks, W. C. (1998). Sulfur in serpentinized oceanic peridotites: Serpentinization processes and microbial sulphate reduction. *Journal of Geophysical Research*, 103, 9917–9929. <https://doi.org/10.1029/98jb00576>
- Alt, J. C., Shanks, W. C., Bach, W., Paulick, H., Garrido, C. J., & Beaudoin, G. (2007). Hydrothermal alteration and microbial sulphate reduction in peridotite and gabbro exposed by detachment faulting at the Mid-Atlantic Ridge, 15° 20' N (ODP Leg 209): A sulfur and oxygen isotope study. *Geochemistry, Geophysics, Geosystems*, 8. <https://doi.org/10.1029/2007gc001617>
- Bağcı, U., Parlak, O., & Höck, V. (2006). Geochemical character and tectonic environment of ultramafic to mafic cumulate rocks from the Tekirova (Antalya) ophiolite (southern Turkey). *Geological Journal*, 41, 193–219.
- Bing-Quan, Z., Yao-Guo, H., Zheng-Wei, Z., Xue-Jun, C., Tong-Mo, D., Guang-Hao, C., et al. (2007). Geochemistry and geochronology of native copper mineralization related to the Emeishan flood basalts, Yunnan Province, China. *Ore Geology Reviews*, 32, 366–380. <https://doi.org/10.1016/j.oregeorev.2006.10.004>
- Brazelton, W. J., Mehta, M. P., Kelley, D. S., & Baross, J. A. (2011). Physiological differentiation within a single-species biofilm fueled by serpentinization. *mBio*, 2. <https://doi.org/10.1128/mbio.00127-11>
- Brazelton, W. J., Schrenk, M. O., Kelley, D. S., & Baross, J. A. (2006). Methane- and sulfur-metabolizing microbial communities dominate the Lost City hydrothermal field ecosystem. *Applied and Environmental Microbiology*, 72, 6257–6270. <https://doi.org/10.1128/aem.00574-06>

- Brazelton, W. J., Thornton, C. N., Hyer, A., Twing, K. I., Longino, A. A., Lang, S. Q., et al. (2017). Metagenomic identification of active methanogens and methanotrophs in serpentinite springs of the Voltri Massif, Italy. *PeerJ*, 5, e2945. <https://doi.org/10.7717/peerj.2945>
- Britten, R. (2017). Regional metallogeny and genesis of a new deposit type-disseminated awaruite (Ni₃Fe) mineralization hosted in the cache creek terrane. *Economic Geology*, 112, 517–550. <https://doi.org/10.2113/econgeo.112.3.517>
- Bruni, J., Canepa, M., Chiodini, G., Cioni, R., Cipolli, F., Longinelli, A., et al. (2002). Irreversible water-rock mass transfer accompanying the generation of the neutral, Mg-HCO₃ and high-pH, Ca-OH spring waters of the Genova province, Italy. *Applied Geochemistry*, 17, 455–474. [https://doi.org/10.1016/S0883-2927\(01\)00113-5](https://doi.org/10.1016/S0883-2927(01)00113-5)
- Canfield, D. E., Raiswell, R., Westrich, J. T., Reaves, C. M., & Berner, R. A. (1986). The use of chromium reduction in the analysis of reduced inorganic sulfur in sediments and shales. *Chemical Geology*, 54, 149–155. [https://doi.org/10.1016/0009-2541\(86\)90078-1](https://doi.org/10.1016/0009-2541(86)90078-1)
- Chamberlain, J. A., McLeod, C. R., Traill, R. J., & Lachance, G. R. (1965). Native metals in the Muskox intrusion. *Canadian Journal of Earth Sciences*, 2, 188–215. <https://doi.org/10.1139/e65-017>
- Cipolli, F., Gambardella, B., Marini, L., Ottonello, G., & Vetuschi Zuccolini, M. (2004). Geochemistry of high-pH waters from serpentinites of the Gruppo di Voltri (Genova, Italy) and reaction path modeling of CO₂ sequestration in serpentinite aquifers. *Applied Geochemistry*, 19, 787–802. <https://doi.org/10.1016/j.apgeochem.2003.10.007>
- Delacour, A., Früh-Green, G. L., Bernasconi, S. M., & Kelley, D. S. (2008). Sulfur in peridotites and gabbros at Lost City (30°N, MAR): Implications for hydrothermal alteration and microbial activity during serpentinization. *Geochimica et Cosmochimica Acta*, 72, 5090–5110. <https://doi.org/10.1016/j.gca.2008.07.017>
- Douglas, P. M. J., Stolper, D. A., Eiler, J. M., Sessions, A. L., Lawson, M., Shuai, Y., et al. (2017). Methane clumped isotopes: Progress and potential for a new isotopic tracer. *Organic Geochemistry*, 113, 262–282. <https://doi.org/10.1016/j.orggeochem.2017.07.016>
- Etiöpe, G., Schoell, M., & Hosgörmez, H. (2011). Abiotic methane flux from the Chimaera seep and Tekirova ophiolites (Turkey): Understanding gas exhalation from low temperature serpentinization and implications for Mars. *Earth and Planetary Science Letters*, 310, 96–104. <https://doi.org/10.1016/j.epsl.2011.08.001>
- Foustoukos, D. I., Bizimis, M., Frisby, C., & Shirey, S. B. (2015). Redox controls on Ni-Fe-PGE mineralization and Re/Os fractionation during serpentinization of abyssal peridotite. *Geochimica et Cosmochimica Acta*, 150, 11–25. <https://doi.org/10.1016/j.gca.2014.11.025>
- Fritz, P., Clark, I. D., Tones, J., Whiticar, M. J., & Faber, E. (1992). Deuterium and ¹³C evidence for low temperature production of hydrogen and methane in a highly alkaline groundwater environment in Oman. Kharaka and Maest. <https://doi.org/10.3917/puf.fritz.1992.01>
- Frost, B. R. (1985). On the stability of sulfides, oxides, and native metals in serpentinite. *Journal of Petrology*, 26, 31–63. <https://doi.org/10.1093/petrology/26.1.31>
- Hannington, M. D., Thompson, G., Rona, P. A., & Scott, S. D. (1988). Gold and native copper in supergene sulphides from the Mid-Atlantic Ridge. *Nature*, 333, 64–66. <https://doi.org/10.1038/333064a0>
- Hosgörmez, H. (2007). Origin of the natural gas seep of Çirali (Chimera), Turkey: Site of the first Olympic fire. *Journal of Asian Earth Sciences*, 30, 131–141. <https://doi.org/10.1016/j.jseaes.2006.08.002>
- Kampschulte, A., & Strauss, H. (2004). The sulfur isotopic evolution of Phanerozoic seawater based on the analysis of structurally substituted sulphate in carbonates. *Chemical Geology*, 204, 255–286. <https://doi.org/10.1016/j.chemgeo.2003.11.013>
- Kelley, D. S., Karson, J. A., Früh-Green, G. L., Yoerger, D. R., Shank, T. M., Butterfield, D. A., et al. (2005). A serpentinite-hosted ecosystem: The lost city hydrothermal field. *Science*, 307, 1428–1434. <https://doi.org/10.1126/science.1102556>
- Kelley, D. S., Karson, J. A., Karson, J. A., Blackman, D. K., Früh-Green, G. L., Butterfield, D. A., et al. (2001). An off-axis hydrothermal vent field near the Mid-Atlantic Ridge at 30° N. *Nature*, 412, 145–149. <https://doi.org/10.1038/35084000>
- Klein, F., & Bach, W. (2009). Fe-Ni-Co-O-S phase relations in peridotite-seawater interactions. *Journal of Petrology*, 50, 37–59. <https://doi.org/10.1093/petrology/egn071>
- Klein, F., Bach, W., Humphris, S. E., Kahl, W.-A., Jöns, N., Moskowicz, B., & Berquo, T. S. (2014). Magnetite in seafloor serpentinite—Some like it hot. *Geology*, 42, 135–138. <https://doi.org/10.1130/G35068.1>
- Klein, F., Bach, W., Jöns, N., McCollom, T., Moskowicz, B., & Berquo, T. (2009). Iron partitioning and hydrogen generation during serpentinization of abyssal peridotites from 15°N on the Mid-Atlantic Ridge. *Geochimica et Cosmochimica Acta*, 73, 6868–6893. <https://doi.org/10.1016/j.gca.2009.08.021>
- Lang, S. Q., & Brazelton, W. J. (2020). Habitability of the marine serpentinite subsurface: A case study of the Lost City hydrothermal field. *Philosophical Transactions of Royal Society A*, 378, 20180429. <https://doi.org/10.1098/rsta.2018.0429>
- Lang, S. Q., Früh-Green, G. L., Bernasconi, S. M., Brazelton, W. J., Schrenk, M. O., & McGonigle, J. M. (2018). Deeply-sourced formate fuels sulphate reducers but not methanogens at Lost City hydrothermal field. *Scientific Reports*, 8, 755. <https://doi.org/10.1038/s41598-017-19002-5>
- Liebmann, J., Schwarzenbach, E. M., Früh-Green, G. L., Boschi, C., Rouméjon, S., Strauss, H., et al. (2018). Tracking Water-Rock Interaction at the Atlantis Massif (MAR, 30°N) Using Sulfur Geochemistry. *Geochemistry, Geophysics, Geosystems*, 19, 4561–4583. <https://doi.org/10.1029/2018gc007813>
- Lorand, J. P. (1987). Cu Fe Ni S mineral assemblages in upper-mantle peridotites from the Table Mountain and Blow-Me-Down Mountain ophiolite massifs (Bay of Islands area, Newfoundland): Their relationships with fluids and silicate melts. *Lithos*, 20, 59–76. [https://doi.org/10.1016/0024-4937\(87\)90024-7](https://doi.org/10.1016/0024-4937(87)90024-7)
- Lorand, J. P. (1989). Mineralogy and chemistry of Cu-Fe-Ni sulfides in orogenic-type spinel peridotite bodies from Ariege (Northeastern Pyrenees, France). *Contribution to Mineralogy and Petrology*, 103, 335–345. <https://doi.org/10.1007/bf04029220>
- Marques, A. F. A., Barriga, F. J. A. S., & Scott, S. D. (2007). Sulfide mineralization in an ultramafic-rock hosted seafloor hydrothermal system: From serpentinization to the formation of Cu-Zn-(Co)-rich massive sulfides. *Marine Geology*, 245, 20–39. <https://doi.org/10.1016/j.margeo.2007.05.007>
- Martin, W., & Russell, M. J. (2007). On the origin of biochemistry at an alkaline hydrothermal vent. *Philosophical Transactions of the Royal Society B*, 362, 1887–1926. <https://doi.org/10.1098/rstb.2006.1881>
- McCollom, T. M. (2007). Geochemical constraints on sources of metabolic energy for chemolithoautotrophy in ultramafic-hosted deep-sea hydrothermal systems. *Astrobiology*, 7, 933–950. <https://doi.org/10.1089/ast.2006.0119>
- McCollom, T. M., Klein, F., Robbins, M., Moskowicz, B., Berquo, T. S., Jöns, N., et al. (2016). Temperature trends for reaction rates, hydrogen generation, and partitioning of iron during experimental serpentinization of olivine. *Geochimica et Cosmochimica Acta*, 181, 175–200. <https://doi.org/10.1016/j.gca.2016.03.002>
- Meyer-Dombard, D. A. R., Woycheese, K. M., Yargıçoğlu, E. N., Cardace, D., Shock, E. L., Güleçel-Pektas, Y., & Temel, M. (2015). High pH microbial ecosystems in a newly discovered, ephemeral, serpentinizing fluid seep at Yanartaş (Chimera), Turkey. *Frontiers in Microbiology*, 5. <https://doi.org/10.3389/fmicb.2014.00723>

- Misra, K., & Fleet, M. E. (1973). The chemical compositions of synthetic and natural pentlandite assemblages. *Economic Geology*, 68, 518–539. <https://doi.org/10.2113/gsecongeo.68.4.518>
- Morrill, P. L., Kuenen, J. G., Johnson, O. J., Suzuki, S., Rietze, A., Sessions, A. L., et al. (2013). Geochemistry and geobiology of a present-day serpentinization site in California: The Cedars. *Geochimica et Cosmochimica Acta*, 109, 222–240. <https://doi.org/10.1016/j.gca.2013.01.043>
- Nan, J., King, H. E., Delen, G., Meirer, F., Weckhuysen, B. M., Guo, Z., et al. (2020). The nanogeochemistry of abiotic carbonaceous matter in serpentinites from the Yap Trench, western Pacific Ocean. *Geology*. <https://doi.org/10.1130/g48153.1.2020>
- Neubeck, A., Sun, L., Müller, B., Ivarsson, M., Hoshgörmmez, H., Özcan, D., et al. (2017). Microbial community structure in a serpentine-hosted abiotic gas seepage at the chimaera ophiolite, Turkey. *Applied and Environmental Microbiology*, 83. <https://doi.org/10.1128/aem.03430-16>
- Pinto, V. M., Hartmann, L. A., & Wildner, W. (2011). Epigenetic hydrothermal origin of native copper and supergene enrichment in the Vista Alegre district, Paraná basaltic province, southernmost Brazil. *International Geology Review*, 53, 1163–1179. <https://doi.org/10.1080/00206810903464547>
- Plümper, O., Botan, A., Los, C., Liu, Y., Malthe-Sørenssen, A., & Jamtveit, B. (2017). Fluid-driven metamorphism of the continental crust governed by nanoscale fluid flow. *Nature Geosciences*, 10, 685–690. <https://doi.org/10.1038/ngeo3009>
- Present, T. M., Adkins, J. F., & Fischer, W. W. (2020). Variability in sulfur isotope records of Phanerozoic seawater sulphate. *Geophysical Research Letters*, 47, e2020GL088766. <https://doi.org/10.1029/2020gl088766>
- Putnis, A. (2009). Mineral replacement reactions. *Reviews in Mineralogy and Geochemistry*, 70, 87–124. <https://doi.org/10.2138/rmg.2009.70.3>
- Putnis, A., & Putnis, C. V. (2007). The mechanism of reequilibration of solids in the presence of a fluid phase. *Journal of Solid State Chemistry*, 180, 1783–1786. <https://doi.org/10.1016/j.jssc.2007.03.023>
- Robertson, A. H. F., & Woodcock, N. H. (1980). Strike-slip related sedimentation in the Antalya Complex, Southwest Turkey. *Special Publication on the International Association of Sedimentologists*, 4, 127–145. <https://doi.org/10.1002/9781444303735.ch8>
- Russell, M. J., Hall, A. J., & Martin, W. (2010). Serpentinization as a source of energy at the origin of life. *Geobiology*, 8, 355–371. <https://doi.org/10.1111/j.1472-4669.2010.00249.x>
- Rye, R. O., Bethke, P. M., & Wasserman, M. D. (1992). The stable isotope geochemistry of acid sulphate alteration. *Economic Geology and the Bulletin of the Society of Economic Geologists*, 87, 225–262. <https://doi.org/10.2113/gsecongeo.87.2.225>
- Sabuda, M. C., Brazelton, W. J., Putman, L. I., McCollom, T. M., Hoehler, T. M., Kubo, M. D. Y., et al. (2020). A dynamic microbial sulfur cycle in a serpentinizing continental ophiolite. *Environmental Microbiology*, 22, 2329–2345. <https://doi.org/10.1111/1462-2920.15006>
- Sakai, H., Marais, D. J. D., Ueda, A., & Moore, J. G. (1984). Concentrations and isotope ratios of carbon, nitrogen and sulfur in ocean-floor basalts. *Geochimica et Cosmochimica Acta*, 48, 2433–2441. [https://doi.org/10.1016/0016-7037\(84\)90295-3](https://doi.org/10.1016/0016-7037(84)90295-3)
- Sánchez-Murillo, R., Gazel, E., Schwarzenbach, E. M., Crespo-Medina, M., Schrenk, M. O., Boll, J., & Gill, B. C. (2014). Geochemical evidence for active tropical serpentinization in the Santa Elena Ophiolite, Costa Rica: An analog of a humid early Earth? *Geochemistry, Geophysics, Geosystems*, 15, 1783–1800. <https://doi.org/10.1002/2013gc005213>
- Schrenk, M. O., Brazelton, W. J., & Lang, S. Q. (2013). Serpentinization, carbon, and deep life. *Reviews in Mineralogy and Geochemistry*, 75, 575–606. <https://doi.org/10.2138/rmg.2013.75.18>
- Schwarzenbach, E. M., Früh-Green, G. L., Bernasconi, S. M., Alt, J. C., Shanks, III, W. C., III, Gaggero, L., & Crispini, L. (2012). Sulfur geochemistry of peridotite-hosted hydrothermal systems: Comparing the Ligurian ophiolites with oceanic serpentinites. *Geochimica et Cosmochimica Acta*, 91, 283–305. <https://doi.org/10.1016/j.gca.2012.05.021>
- Schwarzenbach, E. M., Gazel, E., & Caddick, M. J. (2014). Hydrothermal processes in partially serpentinized peridotites from Costa Rica: Evidence from native copper and complex sulfide assemblages. *Contributions to Mineralogy and Petrology*, 168, 1–21. <https://doi.org/10.1007/s00410-014-1079-2>
- Schwarzenbach, E. M., Gill, B. C., Gazel, E., & Madrigal, P. (2016). Sulfur and carbon geochemistry of the Santa Elena peridotites: Comparing oceanic and continental processes during peridotite alteration. *Lithos*, 252–253, 92–108. <https://doi.org/10.1016/j.lithos.2016.02.017>
- Schwarzenbach, E. M., Gill, B. C., & Johnston, D. T. (2018). Unraveling multiple phases of sulfur cycling during the alteration of ancient ultramafic oceanic lithosphere. *Geochimica et Cosmochimica Acta*, 223, 279–299. <https://doi.org/10.1016/j.gca.2017.12.006>
- Schwarzenbach, E. M., Lang, S. Q., Früh-Green, G. L., Lilley, M. D., Bernasconi, S. M., & Méhay, S. (2013). Sources and cycling of carbon in continental, serpentinite-hosted alkaline springs in the Voltri Massif, Italy. *Lithos*, 177, 226–244. <https://doi.org/10.1016/j.lithos.2013.07.009>
- Shanks, W. C., Bischoff, J. L., & Rosenbauer, R. J. (1981). Seawater sulphate reduction and sulfur isotope fractionation in basaltic systems: Interaction of seawater with fayalite and magnetite at 200–350°C. *Geochimica et Cosmochimica Acta*, 45, 1977–1995. [https://doi.org/10.1016/0016-7037\(81\)90054-5](https://doi.org/10.1016/0016-7037(81)90054-5)
- Shanks, W. C., Böhlke, J. K., & Seal, R. R. (1995). *Stable isotopes in mid-ocean ridge hydrothermal systems: Interactions between fluids, minerals, and organisms*. American Geophysical Union.
- Sunagawa, I. (2005). *Crystals growth, morphology and perfection*. Cambridge University Press. <https://doi.org/10.1017/cbo9780511610349>
- Suzuki, S., Ishii, S., Wu, A., Cheung, A., Tenney, A., Wanger, G., et al. (2013). Microbial diversity in The Cedars, an ultrabasic, ultrareducing, and low salinity serpentinizing ecosystem. *Proceedings of the National Academy of Sciences*, 110, 15336–15341. <https://doi.org/10.1073/pnas.1302426110>
- Taubner, R.-S., Pappenreiter, P., Zwicker, J., Smrzka, D., Pruckner, C., Kolar, P., et al. (2018). Biological methane production under putative Enceladus-like conditions. *Nature Communications*, 9, 748. <https://doi.org/10.1038/s41467-018-02876-y>
- Tutolo, B. M., Mildner, D. F. R., Gagnon, C. V. L., Saar, M. O., & Seyfried, W. E. (2016). Nanoscale constraints on porosity generation and fluid flow during serpentinization. *Geology*, 44, 103–106. <https://doi.org/10.1130/g37349.1>
- Tuttle, M., Goldhaber, M. B., & Williamson, D. L. (1986). An analytical scheme for determining forms of sulfur in oil shales and associated rocks. *Talanta*, 33, 953–961. [https://doi.org/10.1016/0039-9140\(86\)80234-x](https://doi.org/10.1016/0039-9140(86)80234-x)
- Vance, S. D., & Melwani Daswani, M. (2020). Serpentinite and the search for life beyond Earth. *Philosophical Transactions of the Royal Society A*, 378, 20180421. <https://doi.org/10.1098/rsta.2018.0421>
- Zwicker, J., Birgel, D., Bach, W., Richoz, S., Smrzka, D., Grasemann, B., et al. (2018). Evidence for archeal methanogenesis within veins at the onshore serpentinite-hosted Chimaera seeps, Turkey. *Chemical Geology*, 483, 567–580. <https://doi.org/10.1016/j.chemgeo.2018.03.027>